Article

Self-poling of BiFeO thick films

Evgeniya Khomyakova, Matej Sadl, Hana Urši#, John Daniels, Barbara Malic, Andreja Ben#an, Dragan Damjanovic, and Tadej Rojac

ACS Appl. Mater. Interfaces, **Just Accepted Manuscript** • DOI: 10.1021/acsami.6b05885 • Publication Date (Web): 08 Jul 2016

Self-poling of $BiFeO_3$ thick films

Evgeniya Khomyakova,∇,○, Matej Sadl ∇, Hana Ursic ∇, John Daniels §, Barbara Malic ∇, ○, Andreja Bencan ∇, ○, Dragan Damjanovic # and Tadej Rojac ∇, ○*

* Corresponding author

∇ Electronic Ceramics Department, Jozef Stefan Institute, Jamova cesta, 39, Ljubljana, Slovenia

○ Jozef Stefan International Postgraduate School, Jamova cesta, 39, Ljubljana, Slovenia

§ School of Materials Science and Engineering, University of New South Wales, NSW 2052, Australia

Ceramics Laboratory, Swiss Federal Institute of Technology in Lausanne-EPFL, 1015 Lausanne, Switzerland.

Abstract

Bismuth ferrite ($BiFeO_3$) is difficult to pole because of the combination of its high coercive field and high electrical conductivity. This problem is particularly pronounced in thick films. The poling, however, must be performed to achieve a large macroscopic piezoelectric response. This study presents evidence of a prominent and reproducible self-poling effect in few-tens-of-μm-thick $BiFeO_3$ films. Direct and converse piezoelectric measurements confirmed that the as-sintered $BiFeO_3$ thick films yield d_{33} values of up to ~20 pC/N. It was observed that a significant

self-poling effect only appears in cases when the films are heated and cooled through the ferroelectric-paraelectric phase transition (Curie temperature T_C~820 ^oC). These self-poled films exhibit a microstructure with randomly oriented columnar grains. The presence of a compressive strain gradient across the film thickness cooled from above the T_C was experimentally confirmed and is suggested to be responsible for the self-poling effect. Finally, the macroscopic d_{33} response of the self-poled $BiFeO_3$ film was characterized as a function of the driving-field frequency and amplitude.

Key words: Self-poling, Bismuth ferrite, Microstructure, Thick films, Strain gradient

1. Introduction

Perovskite bismuth ferrite, $BiFeO_3$ (BFO), possesses a wide range of prominent and rare characteristics, including an exceptionally high Curie temperature, T_C (~830 ^oC),[1] a large remanent polarization (~100 $\mu C/cm^2$),[2] and a coupling of the magnetic and ferroelectric properties at room temperature.[3,4] These attractive properties can be used in a number of applications, such as transducers, actuators, sensors, data-storage and spintronic devices.[5] Many of these applications require the integration of the BFO onto substrates.

One of the major obstacles to the use of BFO in piezoelectric applications is its high coercive field (50–85 kV/cm),[6-10] which makes the poling of BFO ceramics by the application of external electric fields rather difficult. Typically, electric fields in excess of 120 kV/cm [6-10] are required to pole polycrystalline BFO ceramics and in some cases even higher fields, as high as 1000 kV/cm,[11,12] are applied to BFO thick films, such as those prepared by sol-gel[11] and pulsed-laser-deposition methods[12] with thicknesses in the range of 1 μm. Thus, the poling appears to be

particularly demanding in polycrystalline thick films of BFO,[13-17] although the poling must be performed to obtain a macroscopic piezoelectric activity.

The literature reports cases when as-prepared materials can exhibit macroscopic piezoelectricity without any application of an external electric field; this effect is known as 'self-poling'. Self-poling was investigated in ferroelectric thin films,[18-24] ceramics,[25-27] and single crystals.[28,29] The complexity of the self-poling effect is reflected through a number of diverse, processing-dependent mechanisms that have been proposed to explain this intriguing phenomenon. These include Schottky barriers at the film/electrode interfaces,[18] defective surfaces or interfaces,[29,30] the presence of layers with frozen polarization,[23] chemical composition,[18,31,32] and strain gradients.[21,22,27,33,34] The self-poling reported in epitaxial thin films of $BaTiO_3$,[22,33] $PbZr_{0.2}Ti_{0.8}O_3$[34] and $BiFeO_3$,[21] and that in bulk ceramics of $BiFeO_3$,[27] has been attributed to the presence of strain gradients, which induce poling through, for example, the flexoelectric effect[21,22,33] and/or the redistribution of charged ionic defects.[22,27,33]

Here, we report on a prominent and reproducible self-poling effect in BFO thick films, deposited by screen printing, which is likely driven by the presence of strain gradients throughout the film's thickness. The strain gradient is considered to originate from the substrate-related compressive stresses developing just below the T_C during cooling through the paraelectric-ferroelectric phase transition. The results suggest an alternative way of poling BFO films using a single post-annealing step at a temperature above T_C, overcoming the obstacle of poling BFO "ex-situ" using external electric fields.

2. Experimental section

2.1 Preparation of the thick films

BFO thick films with thicknesses of 6 μm, 17 μm, 23 μm, 30 μm, and 40 μm were prepared using the screen-printing method, as reported in ref.[13] We used Al_2O_3 substrates (99.6%, A-493 Kyocera, Neuss, Germany) with dimensions of 12 mm × 12 mm × 0.6 mm, covered on one of the surfaces with a platinum electrode (herein denoted as Pt/Al_2O_3). The Pt electrode was deposited by screen-printing a commercially available Pt paste (E1192, Ferro Electronic Packaging Materials, Mayfield Heights, Ohio, USA). After printing, the Pt/Al_2O_3 substrates were dried at 150°C and sintered at 1200°C for 1 hour with a 5-K/min heating and cooling rates. The thickness of the platinum electrode was ~15 μm. The BFO thick films were screen printed onto Pt/Al_2O_3, dried and isostatically pressed at room temperature. The thick-film structures were then reactively sintered (reaction and sintering performed during the same annealing step) at 750 °C, 800 °C or 820 °C for 4 hours with heating and cooling rates of 5 K/min. Some samples sintered at 750 °C were additionally heated to 850 °C with short holding time (few minutes) and immediately cooled to room temperature with heating and cooling rates of 5 K/min (subsequently referred to as the post-annealing step).

2.2 Characterization

2.2.1. X-ray diffraction analysis

X-ray diffraction (XRD) analysis was performed at room temperature with an X'Pert PRO MPD diffractometer with Cu–$K_{\alpha 1}$ radiation (PANalytical, Almelo, the Netherlands). The data were collected in the 2θ range from 10° to 78°, in steps of 0.017°, with an integration time of 100 s. The PANalytical X'Pert HighScore software package was used to analyze the XRD patterns. The LaB_6 SRM 660b standard (National Institute of Standards and Technology, Gaithersburg, MD, USA) was used for the calibration of the BFO peak positions. Peakoc software[35] was used

to obtain the normalized intensities of the observed reflections by fitting the peaks with a modified pseudo-Voigt function. The domain-switching fraction, η_{111}, of the BFO thick films was calculated as reported in reference,[36] using the reference intensity values measured on crushed $BiFeO_3$ ceramics prepared by the reactive sintering of Bi_2O_3–Fe_2O_3 at 760 ^oC for 6 hours.

The paraelectric-ferroelectric phase transition of the BFO films was followed by an *in-situ* temperature-dependent XRD analysis using a PANalytical, X'Pert PRO (HTK) diffractometer with Cu–$K_{\alpha1}$ and Cu–$K_{\alpha2}$ radiation in combination with an Anton Paar HTK-1200N oven (Anton Paar, Graz, Austria). The Cu–$K_{\alpha2}$ radiation was stripped using the PANalytical X'Pert HighScore software. The temperature-dependent XRD analysis was performed in two heating and cooling runs in the temperature ranges 780–810 ^oC and 780–840 ^oC with a step of 10 ^oC and heating and cooling rates of 5 K/min (with few-minutes holding time at the individual temperatures required to collect the XRD patterns). The data were collected in the 2θ range from 37^o to 41^o, in steps of 0.026^o, with an integration time of 100 s. All the XRD measurements were performed with the scattering vector perpendicular to the sample surface.

2.2.2 Analytical microscopy

Cross-sections of the BFO thick films were prepared by standard metallographic procedures. The samples were cut, ground with SiC paper and polished with a diamond paste (DP-Paste P 3 μm, 0.25 μm, Struers Inc., Cleveland, USA). After the polishing, the surfaces and cross-sections of the BFO thick films for electron back-scattered diffraction (EBSD) analysis and for atomic force microscopy (AFM) investigations were additionally etched by polishing for ~2 hours using an OP-S suspension (Struers A/S, Ballerup, Denmark).

The microstructures of the thick-film samples were investigated with a scanning electron microscope (SEM) JSM 7600F (Jeol, Tokyo, Japan) equipped with an Inca Energy Detector (energy-dispersive X-ray spectroscopy or EDXS) and EBSD analyzer (Oxford Instruments). All the EDXS analyses were performed at 15 keV. The EBSD analyses were performed using an acceleration voltage of 20 kV, a working distance of 20 mm, a sample tilt angle of ~70^{o} and a 50-μm aperture using an Oxford Instruments HKL Technology CHANNEL 5 software package. The surface and cross-section EBSD mappings were performed on areas of ~28,000 μm^2 and ~15,000 μm^2 with a 0.7-μm step size. To provide electrical conduction at the samples' surfaces and thus prevent charging during the SEM analysis, the samples were coated with carbon prior to analyses using a sputter coater (SCD 050 Sputter Coater, Bal-Tec, Balzers, Liechtenstein).

The average grain size of the films was determined from surface SEM images. To extract the average grain size, areas with more than 370 grains were analyzed and the digitalized microstructure images were processed with the Image Tool software version 3.00 (University of Texas Health Science, San Antonio). The grain size was expressed as the mean Feret's diameter (*d*). The porosity of the films was also evaluated from surface SEM images, i.e., by analyzing a ~2,700 μm^2 area of the sample's surface.

For the transmission electron microscopy (TEM) cross-section investigations, a ~6-μm-thick BFO film on Pt/Al_2O_3 was synthesized and prepared according to the procedure described in ref.[37] High-resolution TEM imaging and selected-area electron diffraction (SAED) analysis were performed on a Jeol JEM-2010F microscope, operated at 200 kV and equipped with a JEOL EDXS detector and a CCD camera.

Piezoresponse force microscopy amplitude images were recorded with an atomic force microscope (AFM; Asylum Research, Molecular Force Probe 3D, Santa Barbara, CA, USA)

equipped with a piezoresponse force mode (PFM). A tetrahedral Si tip coated with Ti/Ir on a Si cantilever coated with Ti/Ir (Asyelec, AtomicForce F&E GmbH, Mannheim, Germany) was used for scanning the polished thick-film surfaces. The Dual AC Resonance Tracking Switching Spectroscopy (DART-SS) mode was used. Out-of-plane amplitude PFM images were measured in the DART mode at 20 V and 305 kHz.

2.2.3. Measurements of the macroscopic piezoelectric response

The as-prepared BFO thick films were characterized in terms of both their direct and converse piezoelectric d_{33} responses. For the direct d_{33} measurements, the upper electrode was painted using a flash-dry silver paint (Spi Supplies Division of Structure Probe, Inc., West Chester, PA, USA). The electrode painting was used to avoid any possible self-poling effect induced by the sputtering of the electrodes.[38] In a second step, we deposited Au and Pt upper electrodes by sputtering circled areas of 1 mm in diameter and re-measured the direct d_{33} response. For the converse d_{33} characterization as a function of the driving-field frequency and amplitude, an upper, sputtered Pt electrode with a diameter of 1 mm was used.

The direct piezoelectric response of the as-sintered BFO thick films was determined using a Berlincourt piezo d_{33} meter (Take Control PM10, Birmingham, UK) at a stress frequency of 200 Hz. The error bars represent the maximum deviation from the average d_{33} value determined by repeated measurements on the same sample.

The converse d_{33} response at weak (sub-coercive) fields was recorded on self-poled samples using a setup based on an optical-fiber sensor, as described in ref.[39] The displacement signals were recorded with an oscilloscope and a lock-in amplifier (the d_{33} and the piezoelectric phase angle were determined from the first-harmonic strain response). The measurements were carried

out at room temperature by applying to the samples a continuous bipolar sinusoidal electric field of selected frequency and amplitude.

3. Results

3.1. Evidence of the self-poling effect in BFO thick films

In the first part of the study we provide evidence of the self-poling effect in ~23-μm-thick BFO films and show that the effect is only large when the BFO film experiences the ferroelectric-paraelectric phase transition. The key role of this phase transition in the self-poling is demonstrated by comparing thick films sintered slightly below (800 °C) and slightly above (820 °C) the Curie temperature. It should be noted that the T_C of the BFO thick films determined here is between 810 ^oC and 820 ^oC, which is ~10 ^oC lower than the T_C reported for BFO bulk ceramics (~830 ^oC).[1,40] Similarly, a deviation in the T_C of the thick films in comparison to the bulk ceramics was also reported for $K_{0.5}Na_{0.5}NbO_3$ (KNN),[41] $PbTiO_3$ (PT)[42] and $0.65Pb(Mg_{1/3}Nb_{2/3})O_3–0.35PbTiO_3$ (PMN-PT)[43] thick films. The origin of the lowered T_C in the films, relative to the ceramics, is complex and multiple, and the slight change of 10 ^oC in the T_C observed here may be a result of a small amount of impurity phases, leading to non-stoichiometric BFO and/or residual stresses in the films (see the following text).

The thick-film structure sintered slightly above the T_C, i.e., at 820 ^oC, exhibited a macroscopic direct piezoelectric response with d_{33}=18±2 pC/N. This was measured on as-sintered films, thus without any prior application of an electric field to the sample. In contrast, the thick film sintered slightly below the T_C, i.e., at 800 ^oC, revealed a much weaker but still a non-zero piezoelectric response (d_{33}=3±1 pC/N). The self-poling effect was confirmed by converse piezoelectric measurements performed after first verifying the self-poling effect with the direct d_{33}

measurements. In this way, the self-poling can be distinguished from any poling that might have occurred due to the application of the electric field during converse measurements.

The converse response of both thick films was analyzed with an oscilloscope and a lock-in amplifier. The measured mechanical displacement signals taken with an oscilloscope as a response to the applied sinusoidal voltage of frequency 10 Hz and amplitude 25 V (corresponding to an electric field amplitude of ~11 kV/cm) are illustrated in the Fig. 1a,b for both samples. The sample sintered at 820 ^{o}C shows a clear piezoelectric response by expanding and shrinking in a sinusoidal form with an amplitude of 0.5 nm, following the waveform of the applied voltage (Fig. 1a). The 180° out-of-phase displacement signal with respect to the voltage signal suggests an in-built polarization in the film directed upwards, thus in the direction from the substrate to the surface of the film, similar to that observed in epitaxial $BaTiO_3$[22,33] and $PbZr_{0.2}Ti_{0.8}O_3$.[34] In contrast, the thick-film structure sintered at 800 ^{o}C did not exhibit any clear periodic displacement signal from the oscilloscope data (Fig. 1b); however, a small, in-phase displacement response with respect to the voltage was detected with the lock-in amplifier, resulting in a d_{33} value of ~2 pm/V. This suggests an in-built polarization pointing in the opposite direction (downward) to that in the 820 °C-sintered film. Within the limits of the measurement techniques, the converse d_{33} measurements were consistent with the direct d_{33} measurements performed using a standard Berlincourt press. Thus, a difference of only 20 ^{o}C in the sintering temperature results in a sharp difference in the amplitude values and the phase of the macroscopic piezoelectric response of the thick films in the as-sintered state.

In order to verify whether the large difference in the d_{33} responses between the two films indeed originates mostly from the self-poling effect, both the samples were poled at room temperature by application of an external DC electric field of 50 kV/cm for ~5 minutes. The

poling field was applied along the thickness of the films both in upward and downward directions with respect to the substrate plane. After the DC poling, the direct piezoelectric d_{33} coefficient of the BFO thick film sintered at 800 ^{o}C was 18±3 pC/N, while that of the sample sintered at 820 °C was 32±3 pC/N. The same values were confirmed for both upward and downward DC poling directions. The results of this experiment imply two conclusions. First, the DC poling significantly improved the macroscopic piezoelectric response of the sample sintered at 800 ^{o}C (d_{33}=3±1 pC/N before DC poling versus d_{33}=18±3 pC/N after DC poling). This confirms that the low d_{33} response of the as-sintered sample at 800 ^{o}C (Fig. 1b) is indeed related to the weak self-poling effect, considering that a much higher d_{33} coefficient can be achieved by the DC poling. Second, the sample sintered at 800 ^{o}C and 820 ^{o}C exhibited very different d_{33} values, i.e., 18±3 pC/N and 32±3 pC/N respectively, despite the same DC field (50 kV/cm) was used for the poling. Such a difference in the macroscopic piezoelectric response can be related to the difference in the microstructure, i.e., different grain size and grain morphology and/or effects of residual stresses, which are discussed in detail subsequently in sections 3.2 and 3.3.

The appearance of the macroscopic piezoelectricity in the as-sintered samples (Fig. 1a and 1b) should be reflected in the preferred alignment of the ferroelectric/ferroelastic domains along the polar $[111]_{pc}$ axis, which we followed by XRD analysis.[36] The XRD patterns of both thick films, i.e., sintered at 820 and 800 ^{o}C, are shown in Fig. 1c,d. respectively. In both samples the perovskite BFO was identified as the major phase with weak reflections of $Bi_{25}FeO_{39}$ (sillenite) secondary phase appearing in the sample sintered at 800 ^{o}C (Fig. 1d). We briefly note here that the absence of the sillenite phase in the sample sintered at 820 ^{o}C may be related to the evaporation of the sillenite phase from the sample surface[6] and/or accelerated reaction of the sillenite phase with the iron-rich counterparts towards BFO formation during sintering at higher

temperature. The thick film sintered at 800 ^{o}C is characterized by the intensity of the $(111)_{pc}$ reflection being lower than that of the $(11\bar{1})_{pc}$ reflection with the $(111)_{pc}/(11\bar{1})_{pc}$ intensity ratio ~1/6 (fig 1d inset). In contrast, the thick-film structure sintered at 820 ^{o}C exhibits a drastic increase in the $(111)_{pc}$ reflection intensity with the $(111)_{pc}/(11\bar{1})_{pc}$ intensity ratio being ~34/1 (Fig. 1c, inset). This suggests an increased volume fraction of the $[111]_{pc}$-oriented domains in the out-of-plane film direction in the sample sintered at 820 °C, which is consistent with the larger macroscopic piezoelectric response of this sample (Fig. 1a) relative to that of the film sintered at 800°C (Fig. 1b).

To evaluate the degree of domain orientation in the two samples, we calculate the volume fraction of the $[111]_{pc}$-oriented domains that were switched from their random orientations to the out-of-plane film direction, η_{111}.[36] In principle, the value of η_{111} lies in the range from –0.25 to 0.75, where the minimum and maximum values correspond to a $[11\bar{1}]_{pc}$ and $[111]_{pc}$ orientation of all the domains in the material in a particular direction, respectively, and $\eta_{111}= 0$ is expected for non-oriented ceramics with a random distribution of domains inside the grains (for example, in unpoled ceramics). For our thick films sintered at 820 ^{o}C and 800 ^{o}C, the calculated η_{111} is 0.73 and –0.08, respectively, indicating a pronounced out-of-plane, $[111]_{pc}$ domain orientation in the sample sintered at 820 ^{o}C and a weak out-of-plane, $[11\bar{1}]_{pc}$ domain orientation in the film sintered at 800 °C.

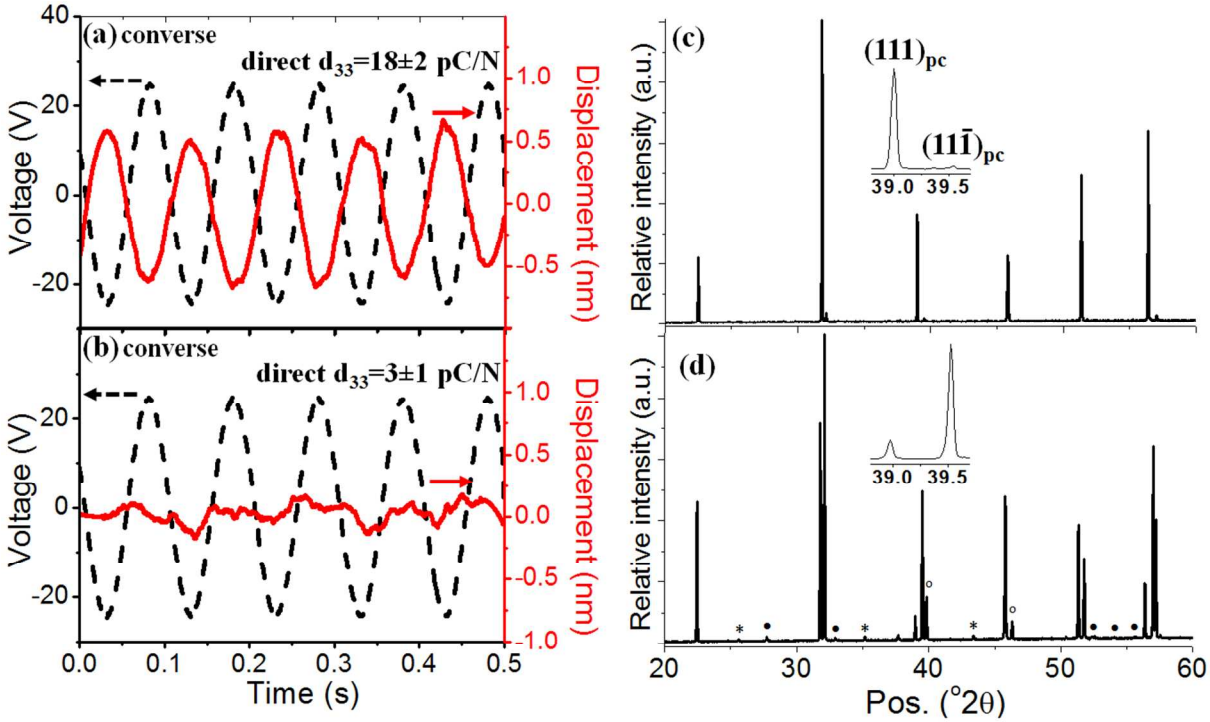

Figure 1: Mechanical displacement of the BFO thick-film structures sintered at 820 °C (a, solid curve) and 800 °C (b, solid curve) as a function of time under an applied sinusoidal voltage (a,b dashed curves). XRD patterns of the BFO thick-film structures sintered at 820 °C (c) and 800 °C (d) with the insets displaying enlarged regions of the $(111)_{pc}$ and $(11\bar{1})_{pc}$ reflections of BFO.

Unmarked peaks are $BiFeO_3$ (PDF No: 01-071-2494); • $Bi_{25}FeO_{39}$ (PDF No: 01-078-1543); peaks denoted with * and ° are related to the Al_2O_3 substrate and the Pt electrode, respectively.

To investigate more directly the implication of the ferroelectric-paraelectric phase transition in the self-poling phenomenon in BFO, we performed an *in-situ* high-temperature (HT) XRD investigation of the sample sintered at 750 °C. The HT XRD analyses were first performed in the temperature range 780–810 °C (Fig. 2a), followed by the analysis in the temperature range 780–840 °C (Fig. 2b). After each cycle, the XRD pattern of the sample was recorded at room temperature (RT).

As shown in Fig. 2, we followed the changes in the structure of BFO with increasing temperature focusing on the $2\Theta^{o}$ region from 38.0 to 40.5° where the $(111)_{pc}$ and $(11\bar{1})_{pc}$ reflections appear. No change from the initial R3c structure was observed in the 780–810 ^{o}C temperature interval (Fig. 2a). On the other hand, the transformation of the crystal structure from the ferroelectric to the paraelectric phase, related to the Curie temperature,[44-46] took place in the temperature range 780–840 ^{o}C (Fig. 2b) (see also the two insets of Fig. 2b). Importantly, just after the transformation from the paraelectric to the ferroelectric phase during cooling, the $(11\bar{1})$ reflection of the ferroelectric phase reduces almost to the noise level, while the intensity of the $(111)_{pc}$ reflection markedly increases (Fig. 2b, bottom inset). Note, however, that just before the transformation to the paraelectric phase during heating, the intensity of the $(11\bar{1})$ was approximately three times higher than that of the $(111)_{pc}$ reflection (Fig. 2b, upper inset). This change of the $(111)_{pc}$-to-$(11\bar{1})_{pc}$ intensity ratio strongly suggests that the domain orientation occurs when the film is cooled just below the T_C (Fig. 2b). This is also supported by the volume fraction of $[111]_{pc}$-oriented domains (η_{111}), calculated from the RT XRD patterns (S1), which are –0.07 for the as-sintered sample, –0.06 after the first HT XRD cycle (refer to Fig. 2a) and 0.71 after the second cycle (refer to Fig. 2b).

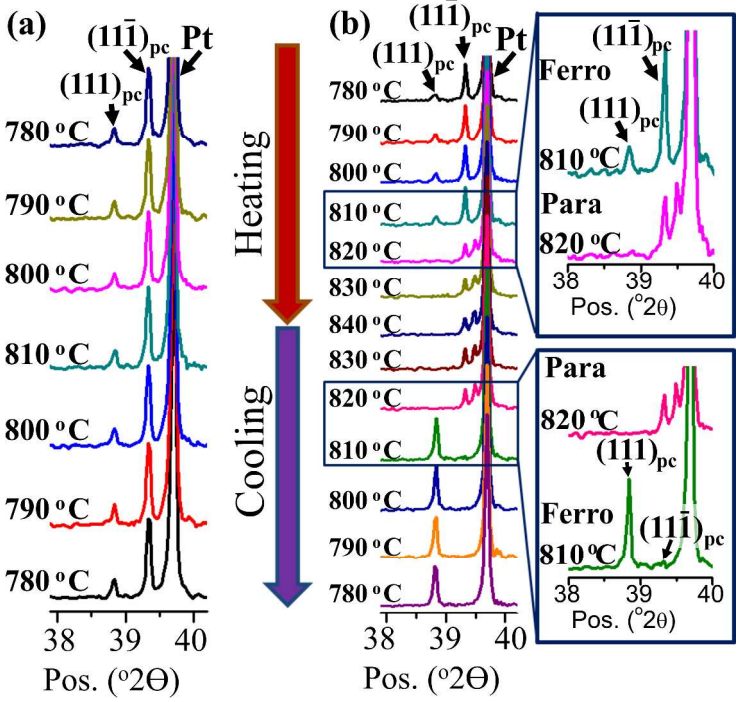

Figure 2: HT XRD investigation of the BFO thick-film structure sintered at 750 °C. XRD patterns recorded in the heating/cooling cycles in the temperature range 780–810 °C (a) and 780–840 °C (b).

The XRD analysis shown in Fig. 2 provides evidence of ferroelastic domain texture in the sample, i.e., non-180° switching of the domains from the in-plane to the out-of-plane thick-film direction; however, such analysis gives no information about the ferroelectric domain texture, i.e., 180° domain switching in either the upward or downward out-of-plane thick-film direction, which is a necessary condition for a non-zero d_{33} response. To confirm the self-poling of the films, we thus measured the direct piezoelectric response of the samples analyzed by HT XRD analysis. The obtained d_{33} values for the as-sintered sample were 0 pC/N, those after the first heating/cooling cycle (up to 810 °C; Fig. 2a) 1±0 pC/N and those for the second heating/cooling cycle (up to 840 °C; Fig. 2b) 20±3 pC/N. The large direct d_{33} measured in samples cooled from

above the T_C (20±3 pC/N) and the corresponding drastic increase in the fraction of the out-of-plane $[111]_{pc}$-oriented domains, occurring during cooling just below the T_C (Fig. 2b, bottom inset), shows clearly that the BFO thick film developed a significant self-poling (d_{33} ~20 pm/V) only after crossing the T_C. The presented experimental results thus confirm that a single post-annealing step (Fig. 2b) or direct sintering (Fig. 1a) above the T_C leads to a strong self-poling effect.

3.2. Microstructure of the BFO thick films

Considering that the XRD analysis and the d_{33} measurements clearly show that the significant self-poling and domain-orientation effects occur upon cooling the films from above the T_C, we analyzed the microstructure of the two samples, i.e., one sintered above (820 °C) and the other below (800 °C) the T_C. The results of the SEM, EBSD and PFM analyses are shown in Fig. 3.

Inspection of the SEM cross-section images of the BFO thick films sintered at 800 ^{o}C (Fig. 3a) and 820 ^{o}C (Fig. 3b) shows that both films contain the perovskite as the main phase, with some inclusions of secondary phases, and that both films are characterized by a similar thickness (~30 μm) and porosity. The total porosity calculated from the SEM images is about 5% for both samples, while the pore size is smaller in the film sintered at 800 ^{o}C (Fig. 3a) compared to the pore size in the film sintered at 820 ^{o}C (Fig. 3b). In addition, EDXS/SEM analyses were also performed and did not reveal any chemical reactions or interdiffusion between the BFO layer and the Pt electrode (not shown here).

EBSD was used to analyze the grain size, grain morphology and crystallographic orientation of the BFO films. The results for the 800 °C-sintered sample are shown in Fig. 3c,d, while those for the 820 °C-sintered sample are shown in Fig. 3e,f,g. Figures 3c-g illustrate the EBSD orientation inverse pole figure (IPF) maps of the cross-sections and surface views of both samples, showing

BFO grains colored by their orientation,[47] and pores or secondary phases as white regions. The film sintered at 800 ^{o}C exhibits a microstructure with several equiaxed grains per film thickness (Fig. 3c). In contrast, the film sintered at 820 ^{o}C possesses coarser columnar grains (Fig. 3e) with clearly visible domains, spanning the entire film thickness (Fig. 3f). The average in-plane grain size in the films sintered at 800 ^{o}C and 820 ^{o}C was evaluated from the SEM surface images (not shown here) and shows a 3-times difference, i.e., 2.6±1.3 μm and 8.7±4.6 μm for, respectively, the 800^{o}C- and 820^{o}C-sintered samples. The increase in the grain size is accompanied by a change in the type of porosity; in the case of the film sintered at 800 ^{o}C, the pores are predominantly intergranular, while in the film sintered at 820 ^{o}C, the majority of the pores are trapped within the grains, indicating that the grain-boundary migration velocity exceeded the pore migration velocity.[48]

The EBSD orientation surface view maps of both thick-film structures, i.e., sintered at 800 ^{o}C (Fig. 3d) and 820 ^{o}C (Fig. 3g), reveal a homogeneous distribution of all the orientations (mapped by the different colors), meaning that no preferred crystallographic orientation of the BFO was observed in any of the thick films, despite the difference in the grain morphology (granular versus columnar). Thus, the film sintered at 820 ^{o}C exhibits columnar, randomly oriented grains in three dimensions, in which, according to the XRD, the domains have a preferred $[111]_{pc}$ orientation (Fig. 1c). The preferred domain orientation was not identified by EBSD; this could be a consequence of the domain re-orientation induced by the mechanical polishing of the sample's surface during the sample preparation for EBSD.

Next, a PFM analysis was used to image the domain morphology in the BFO grains in both samples. The out-of-plane amplitude PFM image of the film sintered at 800 ^{o}C illustrates smaller, below-10-μm-sized BFO grains with submicrometer-sized, irregularly shaped domains

(Fig. 3h and inset). In contrast, the PFM amplitude image of the film sintered at 820 °C shows few-tens-of-micrometer-sized BFO grains with a diverse domain morphology, such as lamellar-type and irregular-shape domains of different sizes (noted in Fig. 3i). As seen from the PFM amplitude image of the surface of this film, some domains percolate through the whole grain (see, for example, the lamellar domain in Fig. 3i). Similarly, the EBSD map revealed domains percolating from the Pt/BFO interface to the film surface (Fig. 3f).

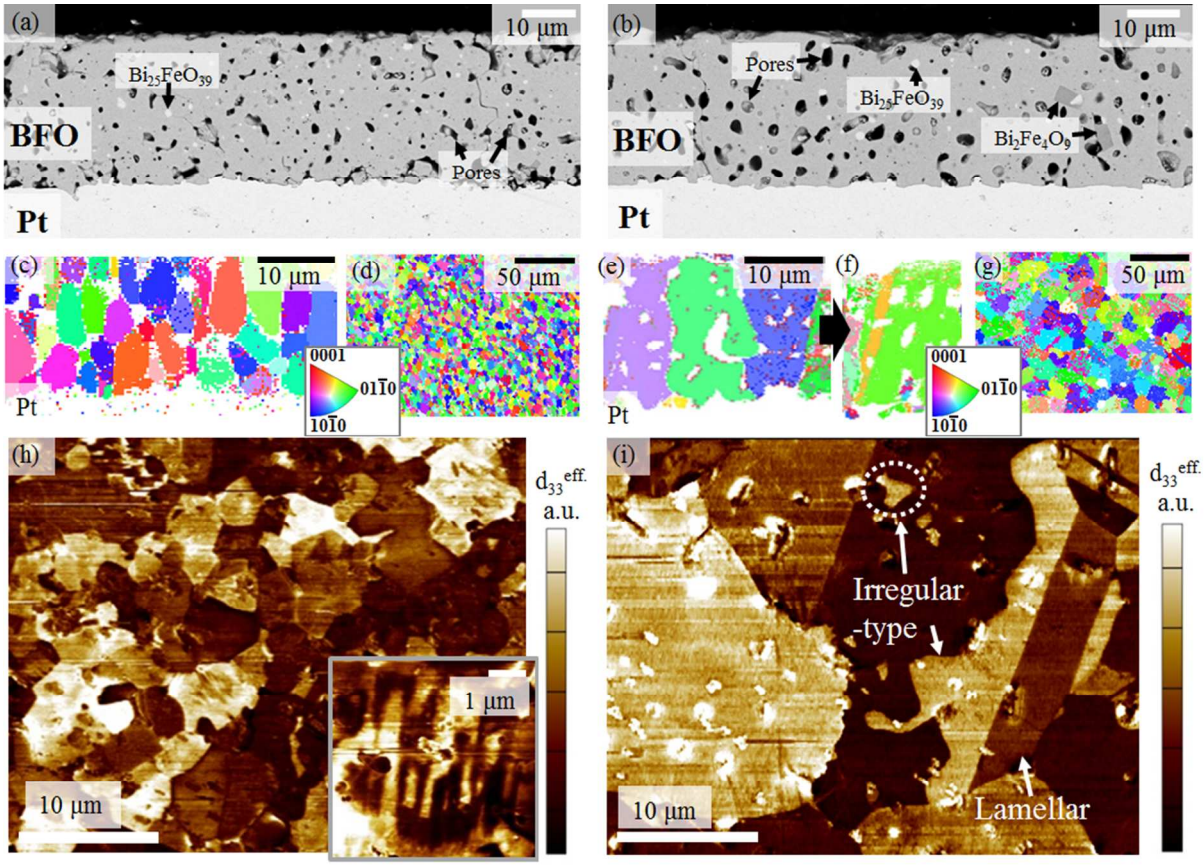

Figure 3: BE-SEM cross-section images of the BFO thick-film structures sintered at 800 °C (a) and 820 °C (b); EBSD orientation map of cross-section (c,e,f) and surface view (d,g) of the BFO thick films sintered at 800 °C (c,d), and 820 °C (e,f,g) with the corresponding color-key IPF legend using the hexagonal R3c BFO symmetry and Miller-Bravais indices (insets). Out-of-plane amplitude PFM images of the BFO thick films sintered at 800 °C (h) and 820 °C (i).

To summarize, the BFO films exhibited a drastic change in microstructure, from equiaxed grains when sintered at 800 ^{o}C (below T_C) to columnar grains when sintered at 820 ^{o}C (above T_C). The same changes in microstructure were observed in the BFO thick films that were sintered below the T_C and just post-annealed above the T_C (S2), which suggests that the microstructural changes are related to the ferroelectric-paraelectric phase transition, regardless whether the film is directly sintered or post-annealed above the transition temperature.

3.3. Strain gradient in the BFO thick films

The strain gradients were proposed to lie at the origin of the self-poling effect in several cases for thin films and bulk ceramics.[21,22,27,33,34] The BFO thick-film structure sintered above the T_C exhibited a significant self-poling effect, thus we used high-resolution (HR) TEM imaging and the selected-area electron diffraction (SAED) technique for an investigation of the change in the unit-cell parameters across the thickness of the sample sintered at 820 ^{o}C.

The HR TEM image of the BFO/Pt interface is illustrated in Fig. 4a where in-plane $[001]_{pc}$ and out-of-plane $[\bar{1}10]_{pc}$ directions of the BFO film (relative to the substrate) are marked. In order to investigate the variation in the unit-cell parameters of the rhombohedral BFO throughout the film thickness, we performed a set of SAED analyses for areas of ~0.5 μm in diameter for one selected domain, as illustrated with circles in the inset of Fig. 4b. The SAED patterns were indexed using a pseudo cubic representation of the BFO unit cell described by the R3c space group; the $(001)_{pc}$ and $(\bar{1}10)_{pc}$ d-values were measured.

The initial thickness of the studied BFO film was 6 μm, which was reduced to 2 μm during the TEM sample preparation. Fig. 4b illustrates the change in the d-spacing along the thickness of a single grain. The change is presented as a relative d/d_0 value, where d_0 is the value obtained from the area closest to the surface of the film, i.e., 2 μm away from the BFO/Pt interface, as indicated in the inset of Fig. 4b. The d/d_0 versus distance clearly demonstrates that the $(001)_{pc}$ and $(\bar{1}10)_{pc}$ interplanar spacings of the BFO reduce towards the BFO/Pt interface by 0.55%. The result thus shows that the unit-cell parameters are not constant across the grain (film) thickness, suggesting the presence of a gradient of compressive strain in both the in-plane and out-of-plane directions relative to the substrate plane. The origin of this triaxial strain is not understood, but it has been reported in the literature for TiN[49,50] and Cu[51] films, and might be associated with the grain-to-grain elastic coupling,[36] particularly because our films are polycrystalline with grains having a random orientation (see EBSD results, Fig. 3c-g).

A strain of 0.55% developing within a distance of ~2 μm results in a strain gradient of $\sim 2.7\times10^{3}$ m^{-1}. It is worth noting that the strain gradient in the BFO thick film is three orders of magnitude smaller than that reported for epitaxial thin films, ($\sim 10^{6}$ m^{-1}),[52] and four orders of magnitude higher than that estimated for bulk ceramics (~ 0.1 m^{-1}).[52]

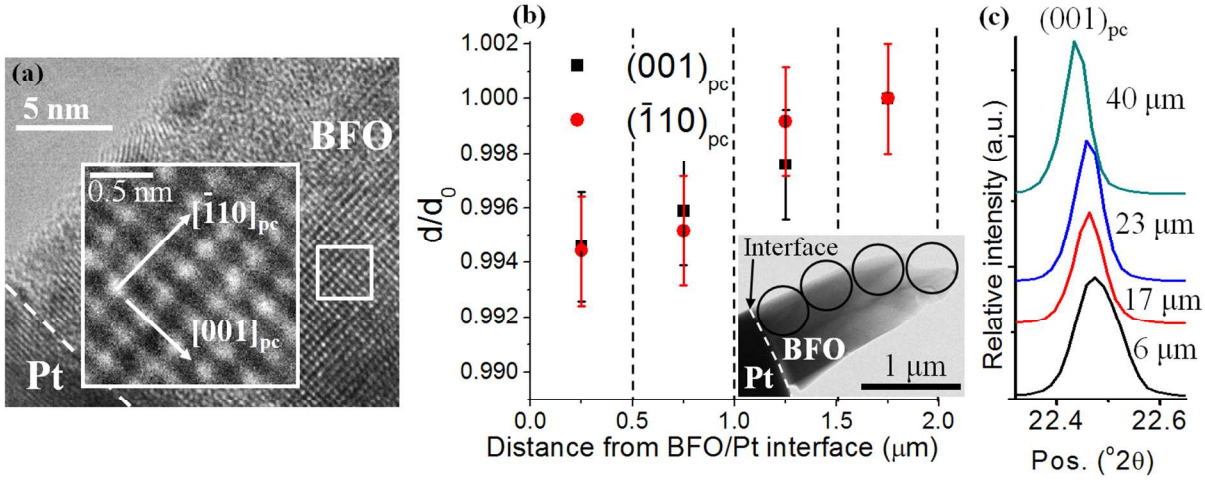

Figure 4: HR TEM image of BFO in the $[110]_{pc}$ zone axis near the film-substrate interface, BFO thick-film structure sintered at 820 °C (a); inset: enlarged marked area showing the out-of-plane $(\bar{1}10)_{pc}$ and in-plane $(001)_{pc}$ directions relative to the substrate plane. Variation of normalized $(001)_{pc}$ and $(\bar{1}10)_{pc}$ d-values calculated from the SAEDs through the film thickness (b), inset: low-magnification BF TEM image of the BFO/Pt interface indicating areas where the SAED patterns were taken. Error bars represent a 0.2% uncertainty evaluated from the stress-free ceramic. The °2Θ region of the XRD pattern showing the $(001)_{pc}$ peak of the BFO film with different thickness (c).

As TEM is a local technique, we additionally studied the change in the out-of-plane unit-cell parameter in differently thick BFO films by XRD analysis. Fig. 4c shows the $(001)_{pc}$ peak of the 6-, 17-, 23- and 40-μm-thick BFO films sintered at 750 °C and post-annealed at 850 °C. The $(001)_{pc}$ peak position is changing with the thickness of the BFO film; the thinner is the BFO layer the more the peak is shifted to the higher °2Θ values, i.e., to the smaller d-spacing. Therefore, a decrease in the out-of-plane BFO unit-cell parameter is observed with the decreasing film thickness. This result is in agreement with the TEM analysis where a decrease in

both the in-plane and out-of-plane d-spacings of the BFO was observed (Fig. 4b) as the substrate was approached. In addition to the change in the peak position, a peak broadening was also observed, which is more significant as the film thickness is reduced (Fig. 4c). This peak broadening is a convolution of effects of microstrain and the reducing thickness of the film.

4. Discussion of the self-poling effect and the piezoelectric behavior of the self-poled BFO thick film

The results confirm a macroscopic direct and converse piezoelectric response in as-sintered BFO thick films where the magnitude and direction of the built-in polarization appears to be dependent on the temperature from which the sample was cooled. BFO thick films cooled from above the T_C exhibit upward polarization and a direct d_{33} of up to 20 pC/N. Worth noting is that this d_{33} value represents 45% of the d_{33} measured for well-poled BFO ceramics, i.e., 44 pC/N,[6] and that this fraction is higher than that observed in thick films of PMN-PT and "soft" PZT (~20–30 %) poled with external electric fields. Consistent with the self-poling effect is the preferred $[111]_{pc}$ domain orientation developing out-of-plane when the film is cooled to just below the T_C (Fig. 2b). In contrast, films that did not experience the ferroelectric-paraelectric phase transition exhibited a weak self-poling effect (Fig. 1b) with a direct d_{33} of 3 pC/N and reversed (downward) polarization (Section 3.1).

The difference in the self-poling effect in the films sintered above and below the T_C may be explained as follows. Self-poled films cooled through the ferroelectric-paraelectric phase transition exhibit a strain gradient of $\sim 2.7\times10^3$ m^{-1} throughout the film thickness (Fig. 4). We propose that the compressive strain gradient originates from the stresses associated with this phase transition. The ferroelectric-paraelectric phase transition of the BFO is strongly first order in nature[44-46] and is accompanied by a large change in the primitive unit-cell volume, i.e., ~1.5%

for a temperature change of 10 K (i.e., during cooling from 830 °C to 820 °C where the $T_C \approx 825$ °C).[44,45] This is two orders of magnitude higher than the volume change expected due to the thermal expansion of the BFO, ~0.03% for a temperature difference of 10 K.[45] This transition-related volume change should result into compressive stresses, since in the BFO film the expansion of the BFO unit cell is hindered due to it being clamped to the substrate once the film is cooled just below the T_C (providing the stresses relax at $T > T_C$). This proposed mechanism is consistent with the compressive strain observed at room temperature in the vicinity of the bottom-electrode/BFO interface (Fig. 4b). Considering that the film is clamped to the substrate, we expect the stresses to decay towards the surface of the film, resulting in a strain gradient, as effectively measured (Fig. 4b).

In the case of the BFO thick film sintered below the T_C, sources of stresses other than those related to the ferroelectric-paraelectric transition should be considered, particularly the stresses induced by the thermal expansion coefficient (CTE) mismatch between the thick film and the substrate material, which are known to have a great impact on the phase composition,[43] crystal structure[41,53] and piezoelectric properties of a thick film.[53] According to the linear CTEs at RT, which are 8.8×10^{-6} K^{-1} for Pt,[54] 7.2×10^{-6} K^{-1} for Al_2O_3,[55] and ~12.2×10^{-6} K^{-1} for BFO,[45] the BFO thick film should be under tensile stress during cooling. The tensile stresses are also substrate-related and might be responsible for the slight orientation of the $[11\bar{1}]_{pc}$ domains in the out-of-plane film direction (Fig. 1d) and weak downward self-poling, although the exact mechanism is not clear. In addition, the observed compressive residual strain in BFO thick films sintered above T_C (Fig. 4b) suggests that the difference in the CTEs is not responsible for the strain state of this film as this mechanism should result in tensile stresses.

While the experimental data presented here strongly suggest a relationship between the significant self-poling in BFO films and the strain gradient, associated with the stresses induced by crossing the ferroelectric-paraelectric phase transition, there are various mechanisms by which the strain gradient may lead to self-poling, for example, through the flexoelectric effect (called flexoelectric poling)[21,56] and/or the redistribution of charged defects.[22,27,33,57] We also note that the observed significant change in the microstructure of the film (from an equiaxed to a columnar grain morphology) by cooling through the T_C (Fig. 3 and S2), can also be a result of the strain distribution in the film and possibly related to the self-poling effect, though the exact mechanisms are still to be investigated.

To compare with the piezoelectric response of BFO ceramics[39] and to gain insights into the domain-wall contributions and the piezoelectric dissipation processes in self-poled BFO films, we next show the longitudinal d_{33} coefficient and piezoelectric phase angle, tanδ, of the BFO thick film sintered at 750 ^{o}C and post-annealed at 840 ^{o}C measured as a function of the frequency and amplitude of the applied electric field (Fig. 5).

The piezoelectric response of the BFO thick film shows a sequence of increasing and decreasing d_{33} and piezoelectric tanδ with the driving frequency (see Fig. 5). Complex piezoelectric dispersions have also been observed in BFO ceramics[39]; however, in that case the d_{33} and piezoelectric tanδ showed larger variations for the same frequency range (1–200 Hz) and driving amplitude (~10 kV/cm). Interestingly, the piezoelectric response of the thick film at low frequency (Fig. 5; inset, 1 Hz) is linear (d_{33} independent on the electric-field amplitude in the range from 4 to 11 kV/cm). This is in contrast to the behavior of BFO ceramics, which exhibit a significant nonlinear response, particularly at low frequencies (< 5 Hz),[39] related to irreversible displacements of the conductive non-180° domain walls. The linear d_{33} response of the BFO film

(Fig. 5; inset) and the weak dispersion in d_{33} (Fig. 5) relative to the BFO ceramics, could be related to the clamping of the film to the substrate, which may provide elastic pinning of the non-180° domain walls, limiting their mobility under an applied field.[58,59] The clamping effect of the substrate is expected to decay from the substrate/film interface towards the surface of the film, which is consistent with the observed strain gradient along the thickness of the film (Fig. 4b). A similar effect of the substrate clamping on the d_{33} response was reported for KNN thick films.[41]

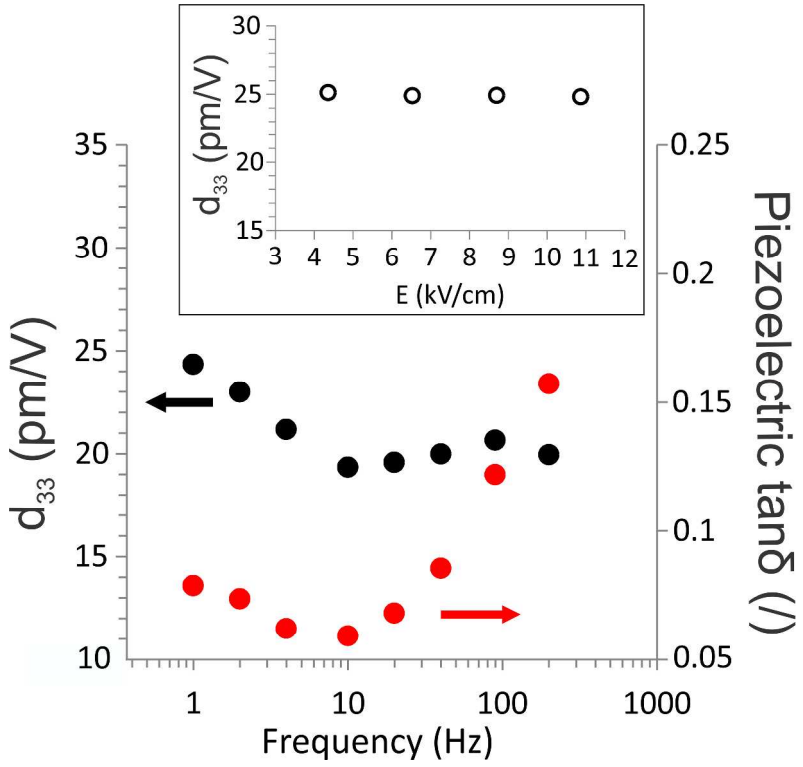

Figure 5: Piezoelectric d_{33} and piezoelectric tanδ (tangent of the phase angle between the mechanical displacement and the electric field) of the BFO thick film sintered at 750 °C and post-annealed at 840 °C as a function of driving-field frequency measured at 10.9 kV/cm of the field amplitude. The inset shows the d_{33} as a function of the amplitude of the driving field measured at 1 Hz.

5. Summary and conclusions

In summary, we report on a self-poling effect in BFO thick films. Through measurements of the direct and converse piezoelectric responses, and an XRD analysis of domain orientation in the films, we present evidence that the self-poling in BFO thick films is tightly linked to the sintering (or post-annealing) temperature and to the strain gradient developed in the film. Significant self-poling only appears when the material is sintered or post-annealed above the T_C (~820^{o}C). Passing through the T_C is also accompanied by an abrupt change in the microstructure: the thick film cooled from above the T_C exhibited a columnar grain morphology, while those cooled from below the T_C had equiaxed grains. The thick films that experienced the ferroelectric-paraelectric phase transition reveal the presence of a compressive strain gradient across the film thickness, which is suggested here to be responsible for the appearance of the self-poling effect. In sharp contrast to BFO ceramics, the macroscopic piezoelectric response of the self-poled BFO film showed a linear, field-independent d_{33} response, possibly related to the clamped state of the film.

Supporting information

XRD, EBSD and SEM analysis of BFO thick films sintered at 750 ^{o}C and post-annealed below or above the Curie temperature. This material is available free of charge via the Internet at http://pubs.acs.org.

Author information

*Corresponding author: Evgeniya Khomyakova

E-mail: evgeniya.khomyakova@ijs.si

Phone: +386 1 477 3583

Post address: Electronic Ceramic Department, Institute Jozef Stefan, Jamova cesta, 39, Ljubljana Slovenia, SI-1000

Acknowledgements

The authors would like to thank Aneja Tuljak, Brigita Kmet, Jena Cilenšek, Silvo Drnovšek for technical support and Slovenian Research Agency (projects P2-0105, PR-05024, J2-5483) for financial support.

References

[1] Moreau, J.M.; Michel, C.; Gerson, R.; James, W.J. Ferroelectric $BiFeO_3$ X-ray and Neutron Diffraction Study. *J. Phys. Chem. Solids.* **1971**, *32*, 1315–1320.

[2] Lebeugle, D.; Colson, D.; Forget, A.; Viret, M. Very Large Spontaneous Electric Polarization in $BiFeO_3$ Single Crystals at Room Temperature and Its Evolution Under Cycling Fields. *Appl. Phys. Lett.* **2007**, *91*, 022907.

[3] Smolenskii, G.; Chupis, I. Ferroelectromagnets. *Sov. Phys. Usp.* **1982**, *25*, 475–493.

[4] Zhao, T.; Scholl, A.; Zavaliche, F.; Lee, K.; Barry, M.; Doran, A.; Cruz, M.P.; Chu, Y.H.; Ederer, C.; Spaldin, N.A.; Das, R.R.; Kim, D.M.; Baek, S.H.; Eom, C.B.; Ramesh, R. Electrical Control of Antiferromagnetic Domains in Multiferroic $BiFeO_3$ Films at Room Temperature. *Nat. Mater.* **2006**, *5*, 823–829.

[5] Catalan, G.; Scott, G.F. Physics and Applications of Bismuth Ferrite. *Adv. Mater.* **2009**, *21,* 2463–2485.

[6] Rojac, T.; Kosec, M.; Budic, B.; Setter, N.; Damjanovic, D. Strong Ferroelectric Domain-Wall Pinning in $BiFeO_3$ Ceramics. *J. Appl. Phys*. **2010**, *108*, 074107.

[7] Su, W.N.; Wang, D.H.; Cao, Q.Q.; Han, Z.D.; Yin, J.; Zhang, R.; Du, Y.W. Large Polarization and Enhanced Magnetic Properties in $BiFeO_3$ Ceramic Prepared by High-Pressure Synthesis. *Appl. Phys. Lett*. **2007**, *91*, 092905.

[8] Chen, F.; Zhang, Q.F.; Li, J.H.; Qi, J.; Lu, C.J.; Chen, X.B.; Ren, X.M.; Zhao, Y. Sol-Gel Derived Multiferroic $BiFeO_3$ Ceramics with Large Polarization and Weak Ferromagnetism. *Appl. Phys. Lett.* **2006**, *89*, 092910.

[9] Zhang, S.T.; Lu, M.H.; Wu, D.; Chen, Y.F.; Ming, N.B. Larger Polarization and Weak Ferromagnetism in Quenched $BiFeO_3$ Ceramics with a Distorted Rhombohedral Crystal Structure. *Appl. Phys. Lett.* **2005**, *87*, 262907.

[10] Yuan, G.L.; Or, S.W.; Wang, Y.P.; Liu, Z.G.; Liu J.M. Preparation and Multi-Properties of Insulated Single-Phase $BiFeO_3$ Ceramics. *Solid State Commun.* **2006**, *138*, 76–81.

[11] Du, P.; Yang, F.; Zang, X.; Qiu, C. Effect of Excess Bi Content on the Electrical Properties of $Bi_{0.95}La_{0.05}FeO_3$ Thick Flms. *J. Mater. Sci.: Mater. Electron.* **2014**, *25*, 5316–5321.

[12] Park, J.M.; Gotoda, F.; Nakashima, S.; Sohgawa, M.; Kanashima, T.; Okuyama, M. Preparation of $BiFe_{0.9}Co_{0.1}O_3$ Films by Pulsed Laser Deposition under Magnetic Field, *Jpn. J. Appl. Phys.* **2011**, *50*, 09NB03.

[13] Khomyakova, E.; Pavlic, J.; Makarovic, M.; Ursic, H.; Walker, J.; Rojac, T.; Malic, B.; Bencan, A. Integration of $BiFeO_3$ Thick Films onto Ceramic and Metal Substrates by Screen-printing. *J. Eur. Ceram. Soc.* **2015**, *35*, 4163–4171.

[14] Das, S.; Basu, S.; Mitra, S.; Chakravorty, D.; Mondal, B.N. Wet Chemical Route to Transparent $BiFeO_3$ Flms on SiO_2 Substrates. *Thin Solid Films.* **2010**, *518*, 4071–4075.

[15] Ryu, J.; Baek, Ch.-W.; Park, D.-S.; Jeong, D.-Y. Multiferroic $BiFeO_3$ Thick Film Fabrication by Aerosol Deposition, *Met. Mater. Int.* **2010**, *16,* 639–642.

[16] Liu, H.; Liu, Z.; Liu, Q.; Yao, K. Ferroelectric Properties of $BiFeO_3$ Films Grown by Sol–Gel Process. *Thin Solid Films.* **2006**, *500,* 105–109.

[17] Ponzoni, C.; Rosa, R.; Cannio, M.; Buscaglia, V.; Finocchio, E.; Nanni, P.; Leonelli, C. Electrophoretic Deposition of Multiferroic $BiFeO_3$ Sub-Micrometric Particles from Stabilized Suspensions. *J. Eur. Ceram. Soc.* **2013**, *33*, 1325–1333.

[18] Afanas'ev, V.P.; Pronin, I.P.; Kholkin, A.L. Formation and Relaxation Mechanisms of the Self-Polarization in Thin Ferroelectric Films. *Phys. Solid State.* **2006**, *48*, 1214–1218.

[19] Kholkin, A.L.; Brooks, K.G.; Taylor, D.V.; Hiboux, S.; Setter, N. Self-Polarization Effect in $Pb(Zr,Ti)O_3$ Thin Films. *Integr. Ferroelectr.* **1998**, *22*, 525–511.

[20] Afanasjev, V.P.; Petrov, A.A.; Pronin, I.P.; Tarakanov, E.A.; Kaptelov, E.Ju.; Graul, J. Polarization and Self-polarization in Thin $PbZr_{1-x}Ti_xO_3$ (PZT) Films. *J. Phys.: Condens. Matter.* **2001**, *13*, 8755–8763.

[21] Jeon, B.Ch.; Lee, D.; Lee, M.H.; Yang, S.M.; Chae, S.Ch.; Song, T.K.; Bu, S.D.; Chung, J.-S.; Yoon, J.-G.; Noh, T.W. Flexoelectric Effect in the Reversal of Self-Polarization and

Associated Changes in the Electronic Functional Properties of $BiFeO_3$ Thin Films. *Adv. Mater.* **2013**, *25*, 5643–5649.

[22] Chen, J.; Luo, Y.; Ou, X.; Yuan, G.; Wang, Y.; Yang, Y.; Yin, J.; Liu, Zh. Upward Ferroelectric Self-Polarization Induced by Compressive Epitaxial Strain in (001) $BaTiO_3$ Films. *J. Appl. Phys.* **2013**, *113*, 204105.

[23] Brinkman, K.; Tagantsev, A.; Muralt, P.; Setter, N. Self Polarization in $Pb(Sc_{1/2}Ta_{1/2})O_3$ Relaxor Thin Films: Impact on the Dielectric and Piezoelectric Response. *Jap. J. Apl. Phys.* **2006**, *45*, 7288–7293.

[24] Kighelman, Z.; Damjanovic, D.; Setter, N. Electromechanical Properties and Self-Polarization in Relaxor $Pb(Mg_{1/3}Nb_{2/3})O_3$ Thin Films. *J. Appl. Phys.* **2001**, *89*, 1393–1401.

[25] Coondoo, I.; Panwar, N.; Bdikin, I.; Puli, V.S.; Katiyar, R.S.; Kholkin, A.L. Structural, Morphological and Piezoresponse Studies of Pr and Sc Co-Substituted $BiFeO_3$ Ceramics. *J. Phys. D: Appl. Phys.* **2012**, *45*, 055302.

[26] Coondoo, I.; Panwar, N.; Rai, R.; Amorín, H.; Kholkin, A.L. Synthesis and Physical Properties of Ca- and Ta-modified $(K,Na)NbO_3$ Lead-Free Piezoelectric Ceramics. *Phase Transit.* **2013**, *86*, 1130–1140.

[27] Chen, X.; Zou, Y.; Yuan, G.; Zeng, M.; Liu, J.M.; Yin, J.; Liu, Zh. Temperature Gradient Introduced Ferroelectric Self-Poling in $BiFeO_3$ Ceramics. *J. Am. Ceram. Soc.* **2013**, *96*, 3788–3792.

[28] Davis, M.; Klein, N.; Damjanovic, D.; Setter, N.; Gross, A.; Wesemann, V.; Vernay, S.; Rytz, D. Large and Stable Thickness Coupling Coefficients of $[001]_C$-Oriented $KNbO_3$ and Li-Modified (K,Na)NbO_3 Single Crystals. *Appl. Phys. Lett.* **2007**, *90*, 062904.

[29] Bdikin, I.K.; Perez, J.A.; Coondoo, I.; Senos, A.M.R.; Mantas, P.Q.; Kholkin, A.L. Ferroelectric Domain Structure of $PbZr_{0.35}Ti_{0.65}O_3$ Single Crystals by Piezoresponse Force Microscopy. *J. Appl. Phys.* **2011**, *110*, 052003.

[30] Wang, B.; Kwok, K.W.; Chan, H.L.W.; Choy, C.L. Internal Field and Self-Polarization in Sol–Gel-Derived Lead Zirconate Titanate Films. *Appl. Phys. A.* **2004**, *79*, 643–646.

[31] Wang, L.H.; Zhao, M.L.; Wang, C.L.; Wang, J.; Kuai, W.J.; Tao, X.T. Piezoelectricity and Local Structural Distortions in $(Na_{0.5}Bi_{0.5})_{1-x}Sr_xTiO_3$-$Bi_{12}TiO_{20}$ Flexoelectric-Type Polar Ceramics. *Appl. Phys. Lett.* **2012**, *101*, 062903.

[32] Kuai, W.J.; Zhao, M.L.; Wang, C.L.; Wang, L.H.; Wang, J.; Gai, Z.G.; Zhang, J.L.; Kuai, N.Y. Effect of Composition on the Structure and Piezoelectricity of $Na_{0.5}Bi_{4.5}Ti_4O_{15}$-Based Flexoelectric-Type Polar Ceramics. *J. Alloy. Compd.* **2013**, *559*, 76–80.

[33] Hou, Y.F.; Zhang, T.D.; Li, W.L.; Cao, W.P.; Yu, Y.; Xu, D.; Wang, W.; Liu, X.L.; Fei, W.D. Self-Polarization Induced by Lattice Mismatch and Defect Dipole Alignment in (001) $BaTiO_3/LaNiO_3$ Polycrystalline Film Prepared by Magnetron Sputtering at Low Temperature. *RSC Adv.* **2015**, *5*, 61821–61827.

[34] Luo, Y.; Li, X.; Chang, L.; Gao, W.; Yuan, G.; Yin, J.; Liu, Zh. Upward Ferroelectric Self-Poling in (001) Oriented $PbZr_{0.2}Ti_{0.8}O_3$ Epitaxial Films with Compressive Strain. *AIP Advances*. **2013**, *3*, 122101.

[35] Peakoc version 1.0; the software written by Olivier Masson, Université de Limoges, Limoges Cedex, France;e-mail: olivier.masson@unilim.fr.

[36] Pramanick, A.; Damjanovic, D.; Daniels, J.E.; Nino, J.C.; Jones, J.L. Origins of Electro-Mechanical Coupling in Polycrystalline Ferroelectrics During Subcoercive Electrical Loading. *J. Am. Ceram. Soc.* **2011**, *94*, 293–309.

[37] Bencan, A.; Tchernychova, E.; Godec, M.; Fisher, J.; Kosec, M. Compositional and Structural Study of a $(K_{0.5}Na_{0.5})NbO_3$ Single Crystal Prepared by Solid State Crystal Growth, *Microsc. Microanal.* **2009**, *15,* 435–440.

[38] Lee, E.G.; Wouters, D.J.; Willems, G.; Maes, H.E. Voltage Shift and Deformation in the Hysteresis Loop of $Pb(Zr,Ti)O_3$ Thin Film by Defects. *Appl. Phys. Lett.* **1996**, *69*, 1223–1225.

[39] Rojac, T.; Ursic, H.; Bencan, A.; Malic, B.; Damjanovic, D. Mobile Domain Walls as a Bridge between Nanoscale Conductivity and Macroscopic Electromechanical Response. *Adv. Funct. Mater.* **2015**, *25*, 2099–2108.

[40] Selbach, S.M.; Tybell, T.; Einarsrud, M.-A.; Grande, T. Phase Transitions, Electrical Conductivity and Chemical Stability of $BiFeO_3$ at High Temperatures. *J. Solid State Chem.* **2010**, *183*, 1205–1208.

[41] Pavlic, J.; Malic, B.; Rojac, T. Microstructural, Structural, Dielectric and Piezoelectric Properties of Potassium Sodium Niobate Thick Films. *J. Eur. Ceram. Soc.* **2014**, *34*, 285–295.

[42] Ryu, J.; Han, G.; Song, T.K.; Welsh, A.; Trolier-McKinstry, S.; Choi, H.; Lee, J.-P.; Kim, J.-W.; Yoon, W.-H.; Choi, J.-J.; Park, D.-S.; Ahn, Ch.-W.; Priya, Sh.; Choi, S.-Y.; Jeong, D.-Y.

Upshift of Phase Transition Temperature in Nanostructured $PbTiO_3$ Thick Film for High Temperature Applications. *ACS Appl. Mater. Inter.* **2014**, *6*, 11980−11987.

[43] Ursic, H.; Hrovat, M.; Holc, J.; Tellier, J.; Drnovsek, S.; Guiblin, N.; Dkhil, B.; Kosec, M. Influence of the Substrate on the Phase Composition and Electrical Properties of 0.65PMN–0.35PT Thick Films. *J. Eur. Ceram. Soc.* **2010**, *30*, 2081–2092.

[44] Arnold, D.C.; Knight, K.S.; Morrison, F.D.; Lightfoot, P. Ferroelectric-Paraelectric Transition in $BiFeO_3$: Crystal Structure of the Orthorhombic β phase. *Phys. Rev. Lett.* **2009**, *102*, 027602.

[45] Selbach, S.M.; Tybell, T.; Einarsrud, M.-A.; Grande, T. The Ferroic Phase Transitions of $BiFeO_3$. *Adv. Mater.* **2008**, *20*, 3692–3696.

[46] Palai, R.; Katiyar, R.S.; Schmid, H.; Tissot, P.; Clark, S.J.; Robertson, J.; Redfern, S.A.T.; Scott, J.F. The β Fhase of Multiferroic Bismuth Ferrite and its γ-β Metal-Insulator Transition. *Phys. Rev. B*. **2008**, *77,* 014110.

[47] Schwartz, A.J.; Kumar, M.; Adams, B.L.; Field, D.P. *Electron Backscattered Diffraction in Material Science*, 2nd ed; Springer: New York, 2009, 35–51, 135.

[48] Brook, R.J.; Pore-Grain Boundary Interactions and Grain Growth. *J. Am. Ceram. Soc.* **1969**, *52*, 56-57.

[49] Abadias, G.; Tse, Y.Y.; Guérin, Ph.; Pelosin, V. Interdependence between Stress, Preferred Orientation, and Surface Morphology of Nanocrystalline TiN Thin Films Deposited by Dual Ion Beam Sputtering. *J. Appl. Phys.* **2006**, *99*, 113519.

[50] Abadias, G. Stress and Preferred Orientation in Nitride-Based PVD Coatings. *Surf. Coat. Tech.* **2008**, *202*, 2223–2235.

[51] Vodnick, A.M.; Nowak, D.E.; Labat, S.; Thomas, O.; Baker, S.P.; Out-of-Plane Stresses Arising from Grain Interactions in Textured Thin Films. *Acta Mater.* **2010**, *58*, 2452–2463.

[52] Lee, D.; Noh, T.W. Giant Flexoelectric Effect through Interfacial Strain Relaxation. *Phil. Trans. R. Soc. A.* **2012**, *370,* 4944–4957.

[53] Han, G.; Ryu, J.; Yoon, W.-H.; Choi, J.-J.; Hahn, B.-D.; Kim, J.-W.; Park, D.-S.; Ahn, Ch.-W.; Priya, Sh.; Jeong, D.-Y. Stress-Controlled $Pb(Zr_{0.52}Ti_{0.48})O_3$ Thick Films by Thermal Expansion Mismatch between Substrate and $Pb(Zr_{0.52}Ti_{0.48})O_3$ Film. *J. Appl. Phys.* **2011**, *110,* 124101.

[54] Touloukian, Y.S.; Kirby, R.K.; Taylor, R.E.; Desai, P.D. *Thermal Expansion: Metallic Elements and Alloys. (Thermophysical properties of matter, Vol. 12.)*, 1st ed; IFI/Plenum: New York, 1975, 254.

[55] Kyocera, Technical characteristics of Al_2O_3, 99.6% purity, A-493 substrate

[56] Garten, L.M.; Trolier-McKinstry, S. Enhanced Flexoelectricity through Residual Ferroelectricity in Barium Strontium Titanate. *J. Appl. Phys.* **2015**, *117,* 094102.

[57] Biancoli, A.; Fancher, C.M.; Jones, J.L.; Damjanovic, D. Breaking of Macroscopic Centric Symmetry in Paraelectric Phases of Ferroelectric Materials and Implications for Flexoelectricity. *Nat. Mater.* **2015**, *14,* 224–229.

[58] Lefki, K.; Dormans, G.J.M.; Measurement of Piezoelectric Coefficients of Ferroelectric Thin-Films. *J. Appl. Phys.* **1994**, *76,* 1764–1767.

[59] Griggio, F.; Jesse, S.; Kumar, A.; Ovchinnikov, O.; Kim, H.; Jackson, T.N.; Damjanovic, D.; Kalinin, S.V.; Trolier-McKinstry, S. Substrate Clamping Effects on Irreversible Domain Wall Dynamics in Lead Zirconate Titanate Thin Films. *Phys. Rev. Lett.* **2012**, *108,* 157604.

Table of Contents Graphic

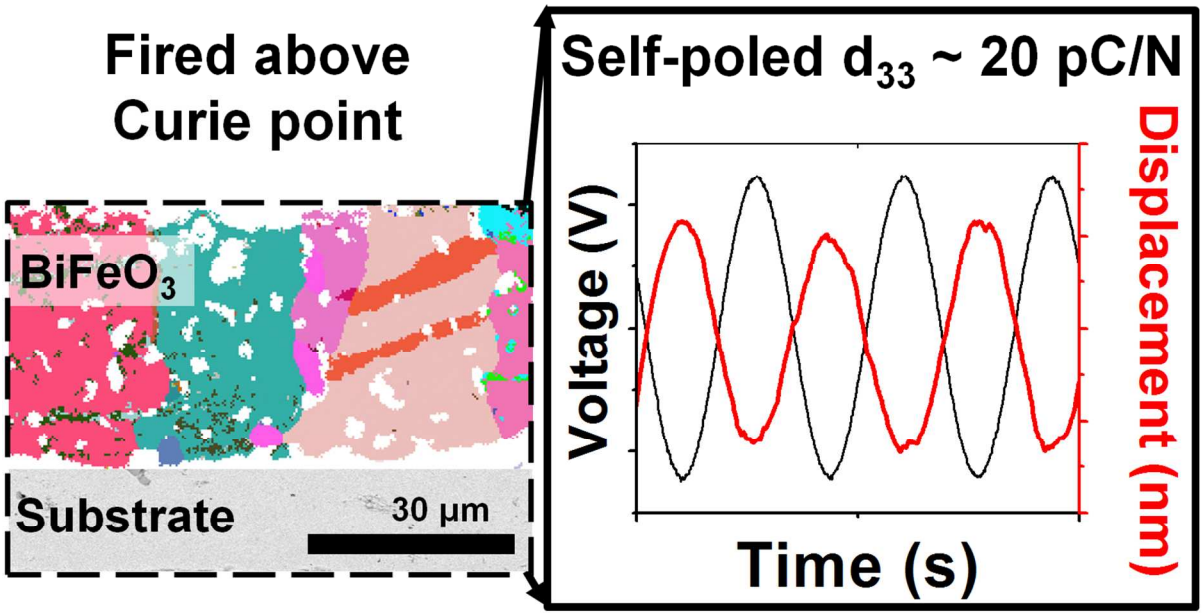

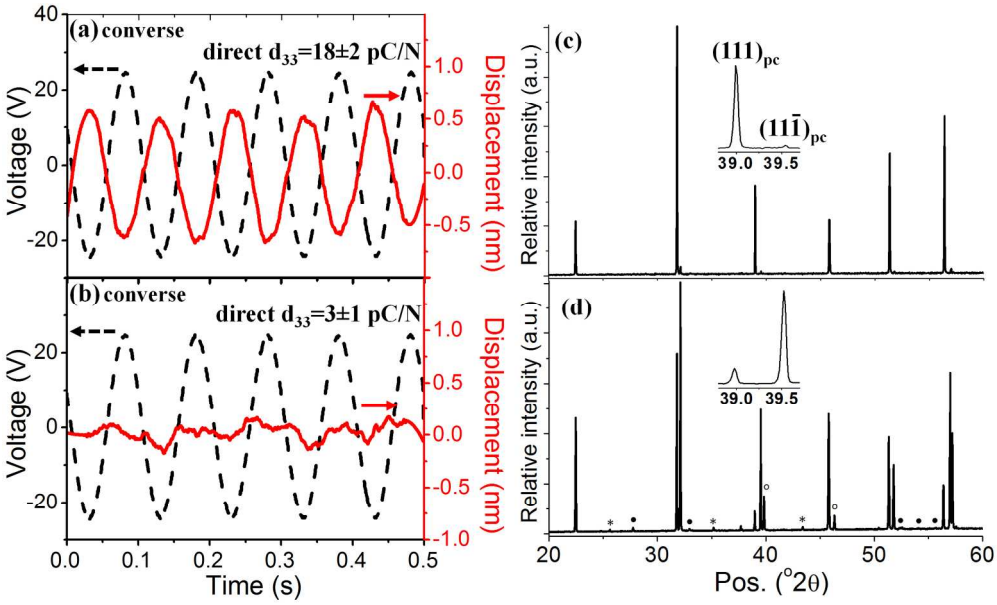

Figure 1: Mechanical displacement of the BFO thick-film structures sintered at 820 °C (a, solid curve) and 800 °C (b, solid curve) as a function of time under an applied sinusoidal voltage (a,b dashed curves). XRD patterns of the BFO thick-film structures sintered at 820 °C (c) and 800 °C (d) with the insets displaying enlarged regions of the $(111)_{pc}$ and $(11\bar{1})_{pc}$ reflections of BFO.
Unmarked peaks are $BiFeO_3$ (PDF No: 01-071-2494); • $Bi_{25}FeO_{39}$ (PDF No: 01-078-1543); peaks denoted with * and ° are related to the Al_2O_3 substrate and the Pt electrode, respectively.
Fig. 1
110x66mm (600 x 600 DPI)

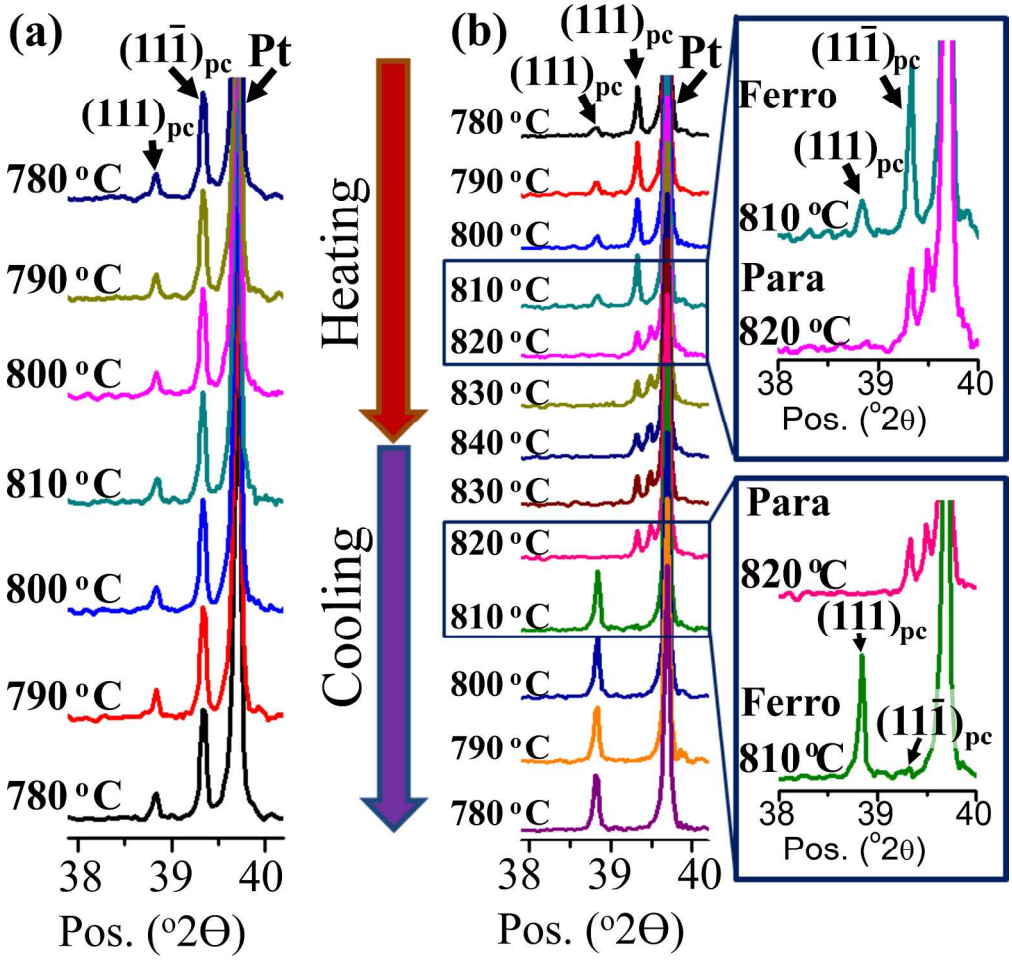

Figure 2: HT XRD investigation of the BFO thick-film structure sintered at 750 °C. XRD patterns recorded in the heating/cooling cycles in the temperature range 780–810 °C (a) and 780–840 °C (b).
Fig. 2
115x110mm (600 x 600 DPI)

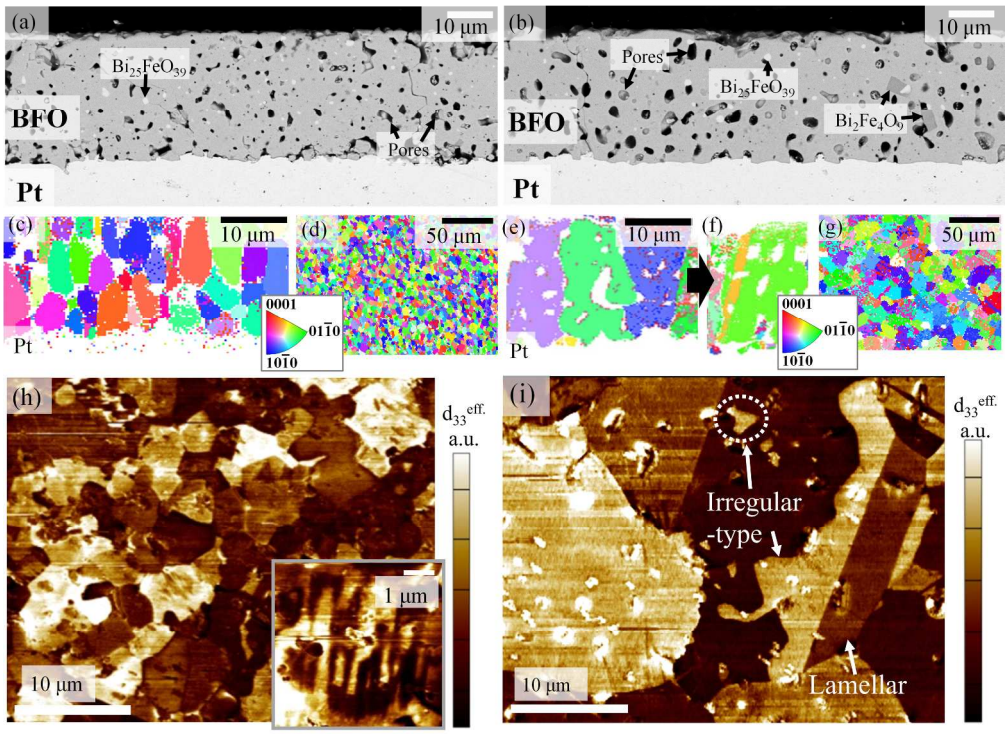

Figure 3: BE-SEM cross-section images of the BFO thick-film structures sintered at 800 °C (a) and 820 °C (b); EBSD orientation map of cross-section (c,e,f) and surface view (d,g) of the BFO thick films sintered at 800 °C (c,d), and 820 °C (e,f,g) with the corresponding color-key IPF legend using the hexagonal R3c BFO symmetry and Miller-Bravais indices (insets). Out-of-plane amplitude PFM images of the BFO thick films sintered at 800 °C (h) and 820 °C (i).

Fig. 3

274x200mm (300 x 300 DPI)

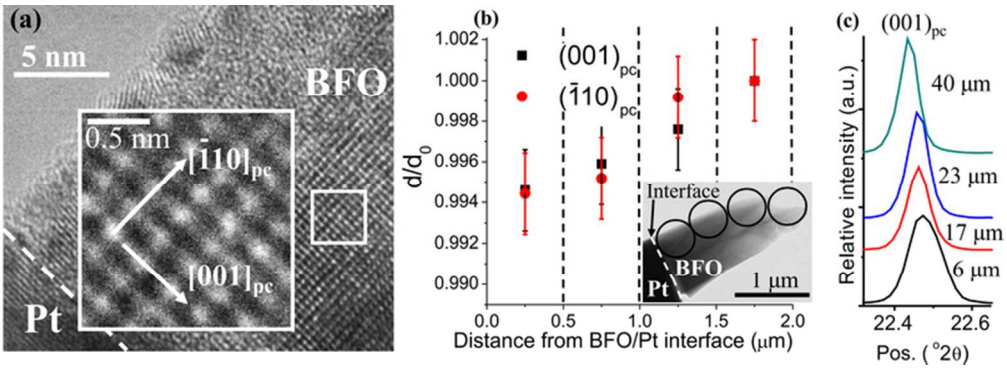

Figure 4: HR TEM image of BFO in the $[110]_{pc}$ zone axis near the film-substrate interface, BFO thick-film structure sintered at 820 °C (a); inset: enlarged marked area showing the out-of-plane $(1\bar{1}0)_{pc}$ and in-plane $(001)_{pc}$ directions relative to the substrate plane. Variation of normalized $(001)_{pc}$ and $(1\bar{1}0)_{pc}$ d-values calculated from the SAEDs through the film thickness (b), inset: low-magnification BF TEM image of the BFO/Pt interface indicating areas where the SAED patterns were taken. Error bars represent a 0.2% uncertainty evaluated from the stress-free ceramic. The °2Θ region of the XRD pattern showing the $(001)_{pc}$ peak of the BFO film with different thickness(c).

Fig. 4

67x24mm (300 x 300 DPI)

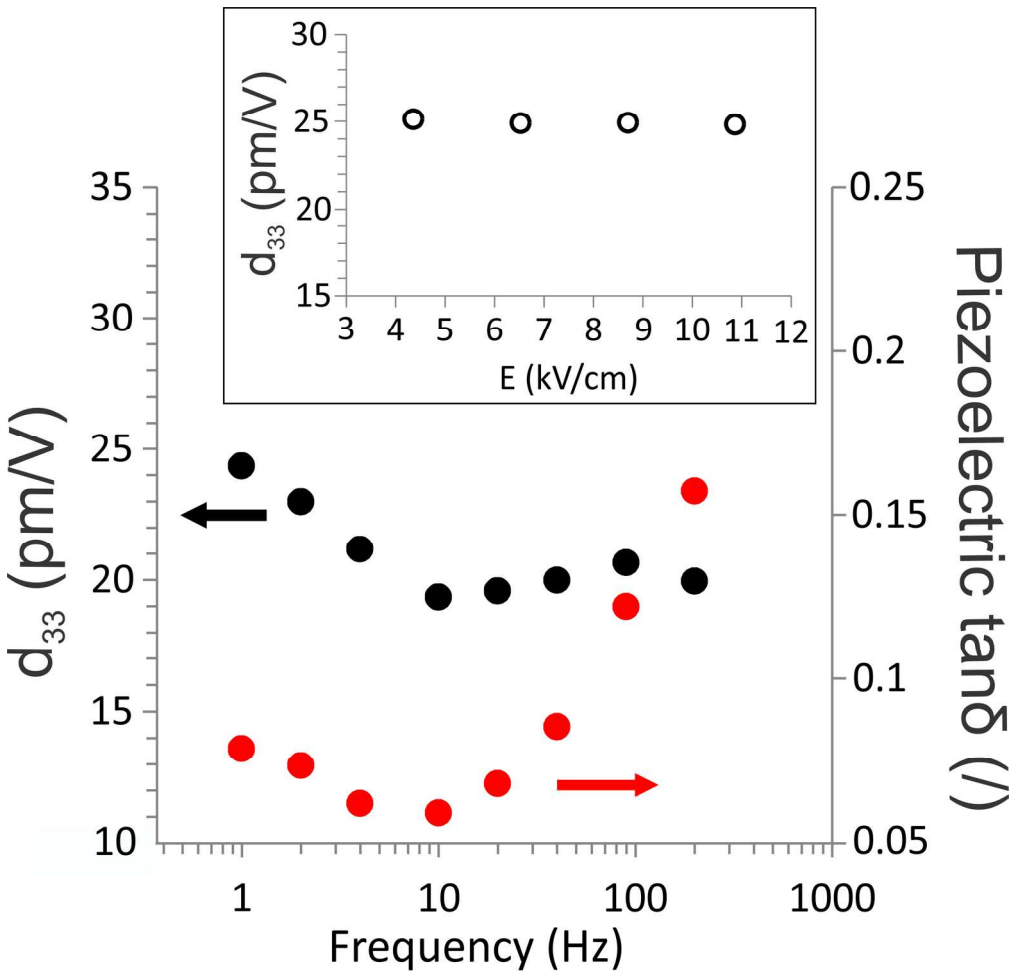

Figure 5: Piezoelectric d_{33} and tanδ of the BFO thick film sintered at 750 °C and post-annealed at 840 °C as a function of driving-field frequency measured at 10.9 kV/cm of the field amplitude. The inset shows the d_{33} as a function of the amplitude of the driving field measured at 1 Hz.

Fig. 5

87x83mm (600 x 600 DPI)